

Can nebular He II emission be explained by ultra-luminous X-ray sources ?

Charlotte Simmonds¹, Daniel Schaerer^{1,2}, and Anne Verhamme^{1,3}

¹ Observatoire de Genève, Département d’Astronomie, Université de Genève, 51 Chemin Pegasi, 1290 Versoix, Switzerland

² CNRS, IRAP, 14 Avenue E. Belin, 31400 Toulouse, France

³ Univ. Lyon, Univ. Lyon1, Ens de Lyon, CNRS, Centre de Recherche Astrophysique de Lyon UMR5574, F-69230, Saint-Genis-Laval, France

September 16, 2021

ABSTRACT

Context. The shape of the ionising spectra of galaxies is a key ingredient to reveal their physical properties and to our understanding of the ionising background radiation. A long-standing unsolved problem is the presence of He II nebular emission in many low-metallicity star-forming galaxies. This emission requires ionising photons with energy > 54 eV, which are not produced in sufficient amounts by normal stellar populations.

Aims. To examine if high mass X-ray binaries and ultra-luminous X-ray sources (HMXB/ULX) can explain the observed He II nebular emission and how their presence alters other emission lines, we compute photoionisation models of galaxies including such sources.

Methods. We combine spectral energy distributions (SEDs) of integrated stellar populations with constrained SEDs of ULXs to obtain composite spectra with varying amounts of X-ray luminosity, parameterised by L_X/SFR . With these we compute photoionisation models to predict the emission line fluxes of the optical recombination lines of H and He+, and the main metal lines of [O III], [O II], [O I], and [N II]. The predictions are then compared to a large sample of low-metallicity galaxies.

Results. We find that it is possible to reproduce the nebular He II $\lambda\lambda 4686$ and other line observations with our spectra and with amounts of L_X/SFR compatible with the observations. Our work suggests that HMBX/ULX could be responsible for the observed nebular He II emission. However, the strengths of the high and low ionisation lines, such as He II and [O I] $\lambda 6300$, depend strongly on the X-ray contribution and on the assumed SEDs of the high energy source(s); the latter are poorly known.

Key words. Galaxies: ISM – Galaxies: high-redshift – X-rays: binaries – Radiation mechanisms: general

1. Introduction

The presence of strong emission lines and the detection of intense UV metal lines in numerous high-redshift galaxies, and more generally the quest for the sources of cosmic reionisation, has re-triggered a strong interest in the physical properties of distant galaxies and their radiation field (see e.g. the review of Stark 2016). In particular, prominent high ionisation spectral features, such as nebular emission in C IV $\lambda 1550$, He II $\lambda 1640$, as well as intense C III $\lambda 1909$ emission, have for example been detected in several $z > 6$ galaxies, raising thus questions about the origin of their hard ionising spectra (Stark et al. 2015; Schmidt et al. 2017). Indeed, galaxies showing these UV emission lines are relatively rare at intermediate redshifts ($z \sim 2 - 3$, see e.g. Erb et al. 2010; Le Fèvre et al. 2019; Schmidt et al. 2021) and in the low- z Universe (see e.g. Senchyna et al. 2017; Berg et al. 2019).

Low- z galaxies showing nebular emission in C IV $\lambda 1550$, He II in the UV (He II $\lambda 1640$) and optical (He II $\lambda 4686$), and other high ionisation lines, such as [Ne V] $\lambda 3426$ are known, primarily among metal-poor star-forming galaxies (Berg et al. 2019; Senchyna et al. 2017; Guseva et al. 2000; Shirazi & Brinchmann 2012). In the IR domain, the fine structure lines of [O IV] $25.9 \mu\text{m}$, [Ne V] $14.3 \mu\text{m}$ and $24.3 \mu\text{m}$, for example, are also detected in certain star-forming galaxies and their strength increases in active galactic nuclei (AGN) (Sturm et al. 2002; Fernández-Ontiveros et al. 2016). The relative weakness and paucity of these lines in star-forming galaxies is not surprising, since neb-

ular C IV $\lambda 1550$, He II $\lambda 4686$, O IV, and Ne V emission lines require photons with energies above 47.9, 54.4, 54.9, and 97.1 eV respectively, which are relatively sparsely emitted by stars and stellar populations and thus thought to be associated with other sources of higher energy photons.

In fact, the presence and strength of nebular He II $\lambda 4686$ in optical spectra (and that of [O IV] in IR spectra) of star-forming galaxies has been recognised already early on as a puzzle/problem (e.g. Schaerer 1996; Guseva et al. 2000; Shirazi & Brinchmann 2012), except in galaxies showing significant populations of Wolf-Rayet (WR) stars, which could be hot and numerous enough to produce sufficient doubly ionised He (He²⁺) (e.g. Schaerer 1996; Schaerer & Stasińska 1999). “Normal” stellar populations do not predict sufficiently hard ionising spectra above 54 eV. Given that WR stars become much rarer at low metallicity ($12 + \log(\text{O}/\text{H}) \lesssim 8.2$), other sources or processes must be found to explain nebular He II emission in these galaxies. Furthermore, nebular He II $\lambda 4686$ is quite ubiquitous at these low metallicities¹, and the average observed intensity He II/H β increases with decreasing O/H. This describes the essence of the nebular He II problem.

Despite constant improvements in stellar evolution and atmosphere models this problem has not yet been solved. Indeed, the nebular He II problem has by large been confirmed by many

¹ For example, in the sample analysed by Schaerer et al. (2019) He II is detected in $\sim 2/3$ of the galaxies. In the larger sample analysed here this is the case for $\sim 1/3$ of the star-forming galaxies.

more recent works using different up-to-date stellar population and photoionisation models, and both analysing the optical and UV recombination lines of He II λ 4686 and He II λ 1640 from different galaxy samples (e.g. Stasińska et al. 2015; Steidel et al. 2016; Nanayakkara et al. 2019; Saxena et al. 2020a; Stanway & Eldridge 2019; Plat et al. 2019; Berg et al. 2021).

On the other hand, various alternate sources and mechanisms have been explored to attempt solving the nebular He II problem. For example, radiative shocks have been proposed to explain (both) the observed He II λ 4686 emission (and [Ne V] λ 3426) in some low-metallicity galaxies (see e.g. Thuan & Izotov 2005; Izotov et al. 2012; Plat et al. 2019). X-rays, from sources such as high-mass X-ray binaries (HMXB) and ultra-luminous X-ray sources (ULX), have been advocated as the origin of nebular He II emission. (e.g. Schaerer et al. 2019; Oskinova et al. 2019). Other authors argued for possible contributions of Pop III-like (metal-free) stars, fast-rotating stars, stripped stars in binary systems or similar, which could boost the emission of He II ionising photons (see Cassata et al. 2013; Szécsi et al. 2015; Göteborg et al. 2019; Stanway & Eldridge 2019). Recently, some studies have also proposed “unconventional” explanations, which do not require additional ionising sources or peculiar stars (Barrow 2019; Pérez-Montero et al. 2020), and which are discussed later (Sect. 4.3). Clearly, no consensus has yet been achieved on the origin of nebular He II, and each of the above scenarios can be debated. Furthermore, several of them do not make any quantitative predictions which can be compared with observations and tested.

In the present paper, we examine the impact of X-ray sources (HMBX, ULX) on nebular He II and other emission lines in a quantitative manner, using Cloudy photoionisation models. Our approach is motivated by the simple model of Schaerer et al. (2019), who compared the observed increase of the X-ray luminosity per unit star-formation rate (L_X/SFR) with decreasing metallicity (Borby et al. 2016; Douna et al. 2015) with the observed increase of the He II/H β intensity, and proposed a causal connection between the two. Such a connection appears quite natural since the X-ray emission in star-forming galaxies is dominated by individual bright sources (HMXB and/or ULX, Mineo et al. 2012) and several ULXs are known to show nebulae with He II emission and also [O IV] 25.9 μ m (Pakull & Angebault 1986; Pakull & Mirioni 2003; Kaaret & Corbel 2009; Berghea & Dudik 2012). Postulating a simple scaling between the He⁺ ionising and X-ray flux taking from observations, Schaerer et al. (2019) have shown that the observed He II/H β intensities and their metallicity dependence can approximately be explained.

Several studies have criticised the recent HMXB/ULX scenario. For example, Kehrig et al. (2021) argued that the observations of the low metallicity galaxy I Zw 18 used by Schaerer et al. (2019) for the scaling, show an insufficient contribution of the ULX in this galaxy to He II ionising photons. New integral field spectroscopic observations with the Keck telescope of I Zw 18 provide a less definite answer on this issue, and Rickards Vaught et al. (2021) argue that shocks or beamed X-ray emission from ULXs could be responsible for the He II emission. Senchyna et al. (2020) report the absence of bright X-ray sources in several nearby galaxies with nebular He II. Furthermore, using simple photoionisation models combining HMXBs described by a multi-colour disc model with normal stellar populations, Senchyna et al. (2020) have concluded that HMXBs are inefficient producers of the photons necessary to power He II.

On the other hand, observations of ULX in nearby galaxies have often revealed the presence of nebulae, some, but not all of them, showing high ionisation emission lines (cf. re-

view of Kaaret et al. 2017). For example, nebular He II λ 4686, [Ne V] λ 3426, and [O IV] 25.9 μ m emission has been observed by Pakull & Mirioni (2003); Lehmann et al. (2005); Abolmasov et al. (2008); Kaaret & Corbel (2009); Berghea et al. (2010); Grisé et al. (2011); Maggi et al. (2011); Moon et al. (2011); Berghea & Dudik (2012); Binder et al. (2018); Urquhart et al. (2018); Vinokurov et al. (2018) in different ULX nebulae, including famous objects such as Holmberg II X-1, NGC5408 X-1, and others. Similarly, nebular He II is also seen in HMXB of lower X-ray luminosity (e.g. Pakull & Angebault 1986). Observationally, HMXB/ULX can thus produce ionising photons which give rise to some or several of the high ionisation lines discussed above and observed in low-metallicity star-forming galaxies. In addition HMXB/ULX are known and predicted to be more numerous/luminous at low metallicities, their contribution is expected to be dominant in distant star-forming galaxies, and L_X/SFR increases towards high redshift (Fragos et al. 2013; Lehmer et al. 2016; Madau & Fragos 2017; Fornasini et al. 2019; Kovelakas et al. 2020). It is therefore of interest to explore the effect of ULXs whose spectra are constrained by observations, on integrated galaxy spectra.

For this purpose we here construct spectral energy distributions (SEDs) of star-forming galaxies including a contribution from ULXs. The stellar spectra, taken from the BPASS binary population synthesis code (Eldridge et al. 2017), are combined with three SEDs of ULX sources with nebulae, and whose spectra have been constrained by multi-wavelength observations by Kaaret & Corbel (2009) and Berghea & Dudik (2012). Combined SEDs are constructed allowing for variable amounts of X-ray luminosities, corresponding to the observed range of L_X/SFR in star-forming galaxies. With these SEDs we compute small grids of Cloudy photoionisation models to predict the most relevant optical emission lines, which are then compared to observations of a large sample of star-forming galaxies for which measurements of nebular He II are available.

Our methodology is described in Sect. 2. In Sect. 3 we present the predicted high ionisation emission line strengths as well as the most important optical emission lines using various emission line diagrams, showing the impact of varying amounts of X-ray emission on these observables. We discuss our results and other recent approaches in Sect. 4. Our main conclusions are summarised in Sect. 5.

2. Photoionisation models of star-forming galaxies including ULXs

To predict the emission line spectra of star-forming galaxies which harbour HMXB or ULX sources, we need to compute detailed photoionisation models using appropriate spectral energy distributions. Since generally the available, theoretical SEDs of galaxies do not include X-ray sources, we first compile several spectra of ULXs from the literature, which we then combine – using an appropriate scaling – with SEDs from evolutionary synthesis models describing the “normal” stellar populations, i.e. excluding the contribution from ULXs. We now briefly describe the SEDs we use, the way they are combined, and the Cloudy model grid we have computed.

2.1. SEDs of ULXs

The SEDs of ULXs are relatively poorly known, and show a large diversity and also variability (e.g. Gladstone et al. 2009; Sutton et al. 2013a,b; Walton et al. 2015; Pintore & Mereghetti

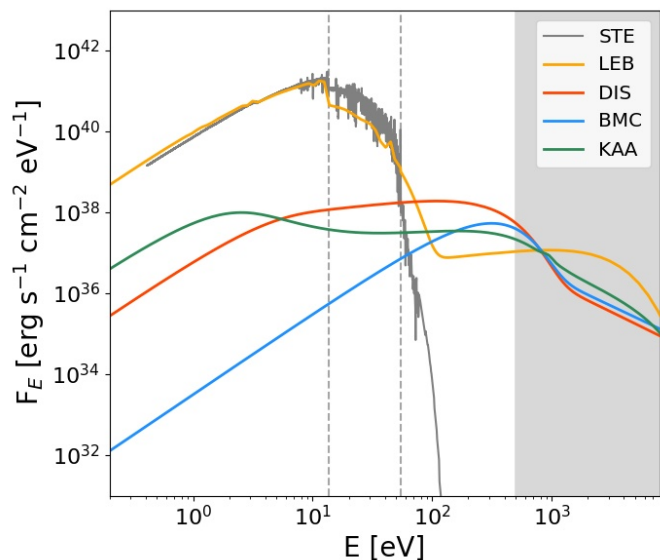


Fig. 1. Basic SEDs used for the photoionisation models: the three ULX spectra (DIS, BMC, KAA), normalised to the same X-ray luminosity L_X , are shown by the red, blue, and green lines respectively. For comparison the pure stellar SED, labelled STE and shown by the grey line, is scaled to our standard value of $L_X/\text{SFR} = 7.9 \times 10^{39} \text{ erg s}^{-1}/(\text{M}_\odot \text{ yr}^{-1})$; see text. The SED of I Zw 18 (LEB model) from Leboutteiller et al. (2017), is shown in yellow, scaled to the same stellar UV flux at $\sim 10 \text{ eV}$ as STE, resulting in an L_X higher by a factor ~ 2.8 compared to the ULX spectra. The vertical dashed lines mark the ionisation potentials of hydrogen and helium (13.6 eV and 54 eV, respectively). The grey shaded area highlights the 0.5-8 keV range of the spectra used for L_X .

2016; Gúrpide et al. 2021b). In general, the X-ray spectra of ULXs is modelled by the sum of two components related to the emission from the accretion flow produced close to the compact object: a multi-colour black body for the accretion disk and a power law representing the coronal emission (Kaaret et al. 2017). Also, the UV/optical spectra can often be fitted by a companion star or an irradiated (sometimes supercritical) disk (cf. Grisé et al. 2012; Tao et al. 2012; Gúrpide et al. 2021a), which further illustrates the uncertainties in the SEDs.

From the literature we have compiled three SEDs of ULXs, which have been observed not only at X-ray wavelengths but also at longer wavelengths (optical, some also in the infrared), and for which tailored photoionisation models fitting the X-ray data and other observational constraints have been constructed. These spectra cover the entire spectral range from the X-rays to the extreme-UV, extending down to low energies ($\sim 54 \text{ eV}$ and lower), which is mandatory to allow combinations with stellar spectra and to explore in particular their impact on He II lines, whose ionisation potential is 54 eV. In particular, throughout this work, we assume that the radiation in the UV-optical regimes is predominantly produced by stars, while the radiation in the X-rays is produced by the ULX. We comment later on the choice and representativeness of these SEDs (Sect. 4.2).

The SEDs used in this paper are shown in Fig. 1, and their main relevant properties, to be discussed below, are summarised in Table 1.

In short, we list two indicators of spectral hardness: the first gives the ratio of the ionising photon fluxes above 54 eV, Q_2 , over those above 13.6 eV, Q_0 , which measures the hardness of the ionising spectrum above the He⁺ potential to that of hydrogen. The second quantity, Q_2/L_X measures the relative number

Table 1. Spectral properties of the basic ULX and stellar SEDs

Model	$\log(Q_0/Q_2)$	$\log(Q_2/L_X)$ [photon/erg]
STE	4.04	-
LEB	2.19	9.50
DIS	-	10.25
BMC	-	9.65
KAA	-	9.61

Notes. *Col. 1:* model name. The stellar model (STE) refers to a metallicity of $12 + \log(\text{O}/\text{H}) = 8.1$. *Col. 2:* ratio between Q_0 and Q_2 . *Col. 3:* ratio between Q_2 and the 0.5-8 keV X-ray luminosity. Empty columns (-) indicate when the SEDs are not or not well defined in one of the spectral ranges considered.

of He⁺ ionising photons emitted per X-ray luminosity (0.5-8 keV in this work), i.e. an efficiency of the X-ray source to produce He II recombination line emission. It is listed only for SEDs with an X-ray component. Q_0/Q_2 is not given for pure ULX SEDs, since their contribution to H-ionisation is negligible in combined models.

2.1.1. NGC 6946 X-1 SEDs

Two SEDs are taken from Berghea & Dudik (2012), who have produced a model for the full optical to X-ray SED of the ULX NGC 6946 X-1 associated to the MF 16 Nebula. This ULX has very similar properties to the famous Holmberg II ULX (e.g. Miller et al. 2005; Goad et al. 2006; Walton et al. 2015) and emission in the infrared nebular [O IV] line, often seen in active galactic nuclei, was detected by Berghea et al. (2010). Several X-ray models were used to reproduce published *Hubble* optical/UV data along with data obtained via X-ray spectroscopy.

Berghea & Dudik (2012) found two XSPEC (Arnaud 1996) Comptonisation models which can fit the X-ray data equally well.

- DISKIR (Irradiated Disk; hereafter DIS): this model represents an accretion disk whose outer region is irradiated by its inner region and the coronal emission of the black hole. A fraction of the bolometric flux of the inner disk is thermalised to the local blackbody temperature at each radius, changing the thermal structure of the outer regions and consequently, the shape of the SED. This model could fit a fraction of the ULXs and was originally presented as a representation of binary black hole systems. In it, the bulk of the disk’s flux is reflected and only the hardest X-ray photons heat the disk (Gierliński et al. 2009).
- BMC (Comptonisation by Relativistic Matter): this is an analytic model that describes the Comptonisation of soft photons by matter undergoing relativistic bulk-motion. It is typically used to describe thermal X-rays which originate in the inner region of an accretion disk in a binary black hole system (Gliozzi et al. 2011), the in-falling matter is heated in the vicinity of the event horizon of the black hole, generating high energy photons (Titarchuk et al. 1997).

These models specifically describe high mass X-ray systems. The difference between these models is found in the predictions they yield for the optical/UV data. Specifically, the BMC model requires a bright stellar companion in order to fit this part of the spectrum of the MF16 nebula, while the DIS model does not. We

include the BMC model without stellar companion to our calculations because we are interested in the high-energy spectrum of the ULX, which will be combined with a stellar population model in order to produce a complete SED. For this work we use both models, BMC and DIS, to which we add stellar emission from the integrated population.

2.1.2. NGC 5408 X-1 SED

The third SED (KAA, hereafter) is a model of a photoionised nebula created by analysing the spectra of the optical counterpart of the ULX NGC 5408 X-1 as described in Kaaret & Corbel (2009). Some authors argue that this source hosts an intermediate-mass black hole candidate, whereas others argue for a stellar-mass compact object accreting at super-Eddington rate (cf. Kaaret & Corbel 2009; Middleton et al. 2011). The spectra of this nebula show high excitation emission lines, in particular He II $\lambda 4686$ and [Ne V] $\lambda 3426$, which suggest X-ray photoionisation (Kaaret & Corbel 2009; Cseh et al. 2012). The KAA SED is based on a Comptonisation model (compps, Poutanen & Svensson 1996) and includes a multi-colour blackbody representing the emission from the wind or the outer parts of the supercritical disk and a cutoff powerlaw as a proxy for the emission emitted closer to the compact object (Gladstone et al. 2009). This model works by using exact numerical solutions to the radiative transfer equation and includes parameters such as geometry, optical depth, electron distribution, spectral distribution of soft seed photons and angle of the observer.

2.2. A galaxy SED including an ULX – I Zw 18

In addition to the above SEDs, which primarily focus on the X-ray part of the spectrum and describe ULXs, we have also used a SED of the well-known metal-poor galaxy I Zw 18, which harbours a ULX source in the centre of its main H II region, I Zw 18-NW. Detailed multi-wavelength observations covering numerous emission lines and tracers from different ISM phases are available for this region. Leboutteiller et al. (2017) have studied this object in depth and demonstrated the importance of the ULX for the understanding of this giant H II region. Their SED for the northwestern region (standard, $L_X = 4 \times 10^{40} \text{ erg s}^{-1}$), including stellar and X-ray emission constructed using multiple, empirically adjusted components and an accretion disk model (diskbb) for the X-ray source, is shown in Fig. 1 and denoted by LEB subsequently. As discussed in Leboutteiller et al. (2017), the SED was empirically adjusted at energies close the He⁺ ionisation potential. Since this is a “combined” and empirically-constrained galaxy SED, covering the entire spectral range (from UV to X-rays) or relevance here, the X-ray contribution is kept fixed.

2.3. Photoionisation modelling using combined SEDs

Finally, to produce complete SEDs including stellar and X-ray emission, we combine the above ULX spectra with SEDs obtained from the binary population synthesis code BPASS v2.1 Eldridge et al. (2017). We adopt the predicted SED of a young population (age 10^6 yr), with a Kroupa IMF allowing for stellar masses up to $100 M_\odot$, and a metallicity of $12 + \log(\text{O}/\text{H}) = 8.1$. In this work we aim to study the effect of the X-ray contribution that ULXs can have over a galaxy, thus, we have focused on one stellar metallicity only, chosen to be representative of our observational sample (cf. below). Small metallicity variations in

Table 2. Model parameters of the Cloudy grid for the “base model”.

Parameter	Values
$\log U$	−1.5, −2.0, −2.5, −3.0, −3.5
$\log((L_X/\text{SFR})/(\text{erg s}^{-1}/(M_\odot \text{ yr}^{-1})))$	38.93, 39.90, 40.63, 40.93, 41.18

Notes. The base model corresponds to a metallicity of $12 + \log(\text{O}/\text{H}) = 8.1$ and $L_X/\text{SFR} = 7.9 \times 10^{39} \text{ erg s}^{-1}/(M_\odot \text{ yr}^{-1})$.

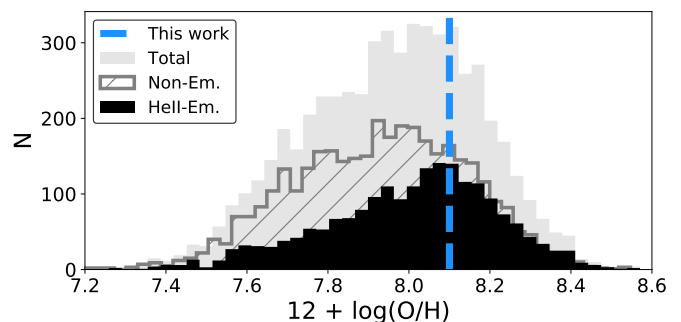


Fig. 2. Metallicity histogram for the observational sample. In black we highlight the distribution of the He II emitters. The vertical dashed line shows our selected metallicity, at $12 + \log(\text{O}/\text{H}) = 8.1$.

the stellar model do not produce significant changes in the SED shape or in the resulting emission line intensities. The young age was chosen for comparison with earlier studies, which commonly use such ages for comparisons with observations (BPT diagrams and others), since this provides relatively hard ionising spectra (see e.g. Kewley et al. 2006; Stasińska et al. 2015; Nakajima et al. 2018). The stellar SED is denoted as STE.

For the combination of ULX and stellar SEDs we are guided by the observed correlation between the X-ray luminosity and star-formation rate (SFR) in star-forming galaxies, which also shows a metallicity-dependence (see e.g. Ranalli et al. 2003; Gilfanov et al. 2004; Laird et al. 2005; Mineo et al. 2014; Brorby & Kaaret 2017). Observations range typically from $L_X/\text{SFR} \sim 10^{39} - 10^{41} \text{ erg s}^{-1}/(M_\odot \text{ yr}^{-1})$, with lower (higher) values at high (low) metallicity. As a standard value we adopt $L_X/\text{SFR} = 7.9 \times 10^{39} \text{ erg s}^{-1}/(M_\odot \text{ yr}^{-1})$ (hereafter called the “base model”), and we explore variations of ± 1 dex or more. To scale the stellar SED we simply use the standard conversion factor between the UV luminosity at 1500 \AA and SFR, given by Kennicutt (1998).

The resulting SEDs are then used as input to the Cloudy photoionisation code of Ferland et al. (2017), version C17.00, to compute a grid of models with varying ionisation parameter with values between $\log U = -1.5$ and -3.5 . This parameter is proportional to the ratio of ionising photons to total hydrogen density, and the range was chosen in order to span the observed range of the main relative line intensities, as commonly adopted in the literature (e.g. Feltre et al. 2017; Ji et al. 2020; Ramambason et al. 2020). The models have a closed geometry and are ionisation bounded, i.e. the calculation stops when the hydrogen ionisation front is reached. We adopt solar abundance ratios from Grevesse et al. (2010), identical stellar and nebular metallicities, and a metallicity of $12 + \log(\text{O}/\text{H}) = 8.1$ for the base model. The range of parameters explored is described in Table 2. In this paper the X-ray luminosity, L_X , refers to the energy range of 0.5–8 keV.

2.4. Observational sample

To compare our models with observations we use a sample of 5607 star-forming galaxies from the Sloan Digital Sky Survey (SDSS) Data Release 14 (Abolfathi et al. 2018) compiled by Y. Izotov and collaborators, analysed in earlier publications (Guseva et al. 2019; Ramambason et al. 2020). The selection criteria used for the extraction of galaxies with active star formation are presented in Izotov et al. (2014). Then we require a detection of the [O III] λ 4363 line with an accuracy better than 4σ , allowing thus direct abundance determinations using the T_e -method. The overall properties of the parent sample from the Data Release 14 are discussed in Guseva et al. (2019).

In Fig. 2 we show the metallicity distribution of the observational sample, and the metallicity of our Cloudy models chosen to be representative of the observations. In this sample, approximately 36 % show nebular He II λ 4686 emission, with a mean He II/H β ratio of $I(\lambda 4686)/I(\text{H}\beta) = 0.011^{+0.007}_{-0.004}$ and a mean metallicity of the He II emitters of $12 + \log(\text{O}/\text{H}) = 8.030^{+0.121}_{-0.158}$. The errors indicate the dispersion of the distributions. In approximately 2/3 of the galaxies He II emission is not detected, with relative intensities below $I(\lambda 4686)/I(\text{H}\beta) \lesssim (2 - 3) \times 10^{-3}$. A smaller, but similarly selected sample of nebular He II emitters has been discussed in Schaerer et al. (2019) and Schaerer et al. (2020).

3. Results

We now present the results from our photoionisation models and compare them to observations.

3.1. Galaxy SEDs including ULXs can produce enough He II emission to explain observations

In Fig. 3 (top panel) we show the predicted He II λ 4686/H β intensity for the Cloudy models using different SEDs, and as a function of L_X/SFR . The range of observed He II λ 4686/H β intensities (when detected) is also shown for comparison. At given L_X/SFR , the highest He II λ 4686/H β intensities are found for the DIS models, followed by BMC, and KAA. This is expected since it reflects the decreasing amount of the He⁺ ionising photons of these SEDs when normalised to the same X-ray luminosity, expressed by Q_2/L_X (see Table 2). The dispersion for a given SED is due to changes in the ionisation parameter, with higher U leading to stronger He II emission. The LEB models with different $\log\langle U \rangle$ are overplotted, showing that the LEB SED can reproduce the observed He II strength. Moreover, the points overlap showing that the variation of $\log\langle U \rangle$ does not make a significant difference in the predicted He II emission. In passing we note that the Cloudy predictions for He II λ 4686/H β for SEDs including X-rays agree or are somewhat lower than the expectations from Case B, as shown in the Appendix.

Finally, He II λ 4686/H β increases with L_X/SFR , since the contribution from X-rays controls the emission of He⁺ ionising photons, which primarily originate from the ULX component (and not from stars).

Compared to observations we find that some of the models predict He II intensities which are strong enough to reach the levels of the observations, i.e. galaxies where nebular He II is detected. Overall, with the ULX SEDs examined here, we find that values of $L_X/\text{SFR} \gtrsim 10^{40} \text{ erg s}^{-1}/(\text{M}_\odot \text{ yr}^{-1})$ are required to reach currently detectable levels of He II λ 4686 emission. There are several ways to explain the absence of He II emission, well below the threshold of the current observations (He II λ 4686/H $\beta \lesssim 0.005$). Indeed, even in the presence of ULXs

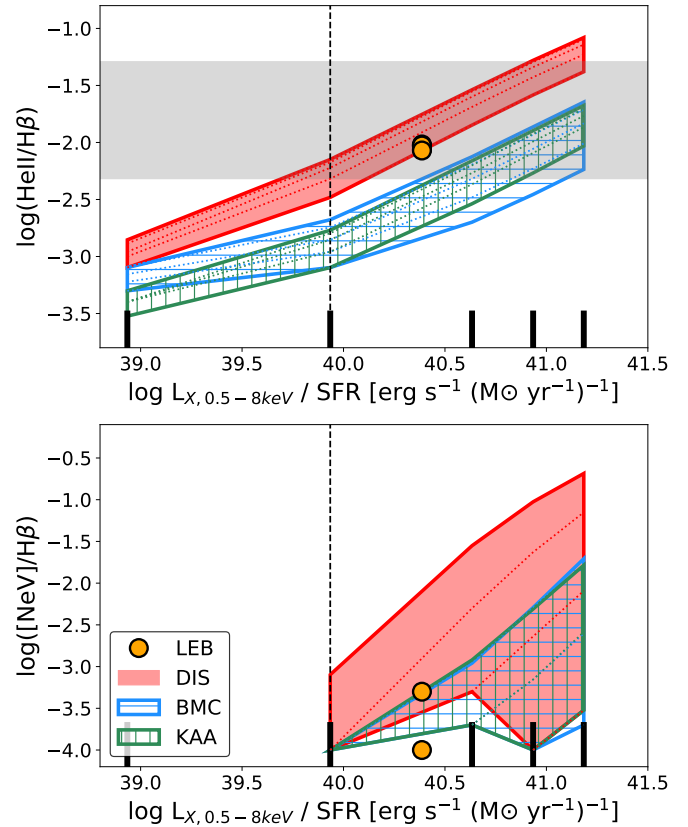


Fig. 3. Predicted relative emission line intensity ratios of nebular He II λ 4686 (top) and [Ne V] λ 3426 (bottom) as a function of L_X/SFR for different SEDs. Each colour represents a different X-ray model. The horizontal gray area shows the typical range of the observed He II line intensity, when detected. The vertical dashed line indicates the L_X/SFR value of our "base model". The dispersion in each SED model is due to changes in the ionisation parameter. It can be seen that an increase of the X-ray component produces stronger He II emission, overlapping with the observational area for $L_X/\text{SFR} \approx 10^{40} - 10^{41} \text{ erg s}^{-1}/(\text{M}_\odot \text{ yr}^{-1})$, depending on the adopted ULX SED. For comparison, the value for the LEB models are overplotted, showing that the LEB SED can reproduce the observed He II strength. In approximately 2/3 of the galaxies He II emission is not detected, with relative intensities below $I(\lambda 4686)/I(\text{H}\beta) \sim (2 - 3) \times 10^{-3}$. The models with $L_X/\text{SFR} < 10^{40} \text{ erg s}^{-1}/(\text{M}_\odot \text{ yr}^{-1})$ do not produce significant [Ne V] emission (i.e. $I([\text{NeV}])/I(\text{H}\beta) < 10^{-4}$), and are therefore omitted.

or other X-ray sources, the diversity of their intrinsic properties (SEDs in particular) and variations in the ionisation parameter can cause very weak or no He II emission. More detailed comparisons with observations, involving also other emission lines will be discussed below.

3.2. [Ne V] emission and its relation with He II

In addition to He II, a few blue compact dwarf galaxies show [Ne V] λ 3426 emission (Izotov et al. 2004; Thuan & Izotov 2005; Izotov et al. 2012). Given its high ionisation potential of 97.1 eV, this line is often associated to hard non-thermal radiation from AGN, making its detection in star-forming galaxies interesting to explore. The study of Izotov et al. (2012) lists in total eight low-metallicity star-forming galaxies with intensities $[\text{Ne V}]\lambda 3426/\text{He II}\lambda 4686 \sim 0.2 - 0.5$, which they propose can be explained by fast radiative shocks contributing ~ 10 per cent

of the stellar ionising (Lyman continuum) flux. We attempt to explain these observations with our models.

In Fig. 3 (bottom panel) we show the predicted [Ne v] λ 3426 line intensity. As expected, for a given L_X/SFR the highest [Ne v] λ 3426/H β intensities are again found in the DIS model, followed by BMC and KAA. This is analogous to the case of He II/H β , and is explained by the decreasing amount of Ne⁴⁺ ionising photons in the different SEDs. Compared to He II/H β , however, the [Ne v] line intensity decreases more rapidly with decreasing L_X/SFR , and a higher L_X/SFR is needed in order to produce [Ne v] emission with comparable (and detectable) intensities as He II λ 4686. Finally, the [Ne v] emission depends strongly on the ionisation parameter (as expected for forbidden lines), in contrast to the He II recombination lines, and significant emission is only predicted for models with high U ($\log U = -1.5$ to -2.5). The observed intensities, reaching up to [Ne v] λ 3426/H β = 0.0091 ± 0.0031 in galaxies with strong He II λ 4686/H β ~ 0.03 (Izotov et al. 2012) are well reproduced by our models. The strong dependence of the [Ne v] line on U (primarily) and variations in SED shape can also naturally explain why only a (small) fraction of He II emitters also show [Ne v].

3.3. The impact of ULXs on emission line diagnostics

To examine the effect of the high energy part of the SED on the optical emission lines we reproduce line ratio diagrams probing three ionisation stages of oxygen, the strength of nebular He II, and two classical BPT diagrams (Baldwin et al. 1981) involving oxygen and nitrogen lines. Figure 4 shows four different representations of the results: [O III]/[O II] versus [O I]/[O III] and He II/H β on the left panels, and BPT on the right panel. Several of these diagrams were also discussed and compared to the same observational sample in Stasińska et al. (2015) and Ramambason et al. (2020). As shown in Fig. 4, and well known, the ionisation parameter U determines basically the observed [O III]/[O II] ratio, and overall also [O III] λ 5007/H β (cf. Kewley et al. 2006). Then, at fixed U , the addition of X-rays leads primarily to an increase of He II λ 4686/H β as shown above (Fig. 3), by up to three orders of magnitudes for the model SEDs and maximum L_X/SFR value considered here. The low energy tail of the X-ray emission does not only create a central He²⁺ region from which the He II recombination lines are then emitted. The large mean free path of the soft X-ray photons also leads to an extension of the H II region in the outer parts, causing thus stronger emission from low ionisation lines emitted in these regions. This explains the increase of [O I] λ 6300/H α also shown in this figure. As expected, the harder the spectra – as measured by Q_2/Q_0 – the higher is the maximum intensity of both He II λ 4686/H β and [O I] λ 6300/H α . Other lines such as [N II] are not significantly affected by X-rays, because the [N II] lines are formed in more central regions of the nebula.

The comparison of the models with the observations plotted in Fig. 4 shows that the combination of stellar and ULX SEDs allows to cover basically the entire range of emission line ratios, including He II/H β as already shown in Fig. 3. The [N II] λ 6548,6584/H α BPT diagram is well reproduced, i.e. our models follow the observational sample, which is in particular due to an appropriate N abundance for this sample. The purely stellar models and those with low amounts of X-rays do somewhat underpredict the [O I] λ 6300 emission, as also seen in other studies (Stasińska et al. 2015; Plat et al. 2019; Ramambason et al. 2020). Interestingly, the addition of X-rays allows simultaneously to reach the observed intensities of He II λ 4686 and a slight “boost”

of [O I] λ 6300 to potentially reconcile these different line ratios in a consistent manner, which is further illustrated in Fig. 5. However, alternative explanations for the possible discrepancies of [O I] λ 6300 and other low ionisation lines, which are not related to high energy emission, exist (see e.g. Stasińska et al. 2015; Ramambason et al. 2020).

4. Discussion

The above results are promising, showing that the presence of ULXs in star-forming galaxies can – in some conditions – explain the observed emission of nebular He II and other lines in low metallicity galaxies. We now discuss these conditions and related assumptions, other studies on the contribution of ULXs/HMXBs, and other approaches to tackle this problem.

This work has shown that X-ray emission can drive the nebular He II emission by using ULX/HMXBs as the sources of the observed high energy radiation. In particular, we found that the model DIS yields the most promising results. In low metallicity galaxies HMXBs are expected to outnumber low mass X-ray binaries by a factor of ~ 10 (Douna et al. 2015). Additionally, about 2/3 of the $L_{X,0.5-8keV}$ per unit SFR is expected to be due to HMXBs (Mineo et al. 2014). If HMXBs are indeed responsible for the nebular He II emission, the excess of these objects at lower metallicity would agree with the observations.

4.1. The ULX/HMXB – He II connection in the literature

Our study follows up on the scenario proposed by Schaerer et al. (2019) and Schaerer et al. (2020), who relate the observed anticorrelation between integrated L_X/SFR and metallicity of star-forming galaxies (Douna et al. 2015; Brorby et al. 2016; Lehmer et al. 2021) to the same observed trend of nebular He II λ 4686/H β with metallicity. They show that the observations can roughly be reproduced with simple assumptions and an empirical calibration of $Q_2/L_X = (1 - 3) \times 10^{10}$ photon erg^{-1} based on the ULX observed in the low-metallicity galaxy I Zw 18. This work postulates that X-ray bright sources (HMXB, ULX) are the main source of He⁺ ionising photons in low-metallicity galaxies.

Overall, the present work builds on the same assumptions, using, however, detailed SEDs of ULX to perform quantitative photoionisation models to predict not only the He⁺ and H recombination lines, but also metallic forbidden lines, which are successfully compared to the observations. In particular, our Cloudy models can reproduce the observed intensities of the high ionisation lines of He II, [Ne v] λ 3426, as well as the lines of [O III], [O II], and [O I]². Observationally, Saxena et al. (2020a,b) have explored the X-ray emission from a sample of 18 He II emitters and a comparison sample of non-He II emitters at redshift $z \sim 3$ by stacking, finding similar ratios of L_X/SFR for both samples. From this they conclude that X-ray binaries or weak or obscured AGN are unlikely to be the dominant producers of He⁺ ionising photons in star-forming galaxies at this redshift. For the 18 He II emitters available for this study they obtain a stacked $\log \langle L_X \rangle / \langle SFR \rangle = 40.01^{+0.26}_{-0.75}$ (in $\text{erg s}^{-1}/(M_\odot \text{ yr}^{-1})$) at $z = 3.04$, and $39.95^{+0.12}_{-0.17}$ for the non-emitters at $z = 3.15$. Both values are compatible with existing measurements at $z \sim 1.5 - 2.3$ (Fornasini et al. 2019). However, the uncertainties on L_X/SFR are quite large, especially for the He II emitters, and the L_X/SFR of both samples is not significantly larger than the average value observed in the low- z Universe at

² Since observations probing O IV lines are quite rare, we are currently not able to examine this ionisation stage as well.

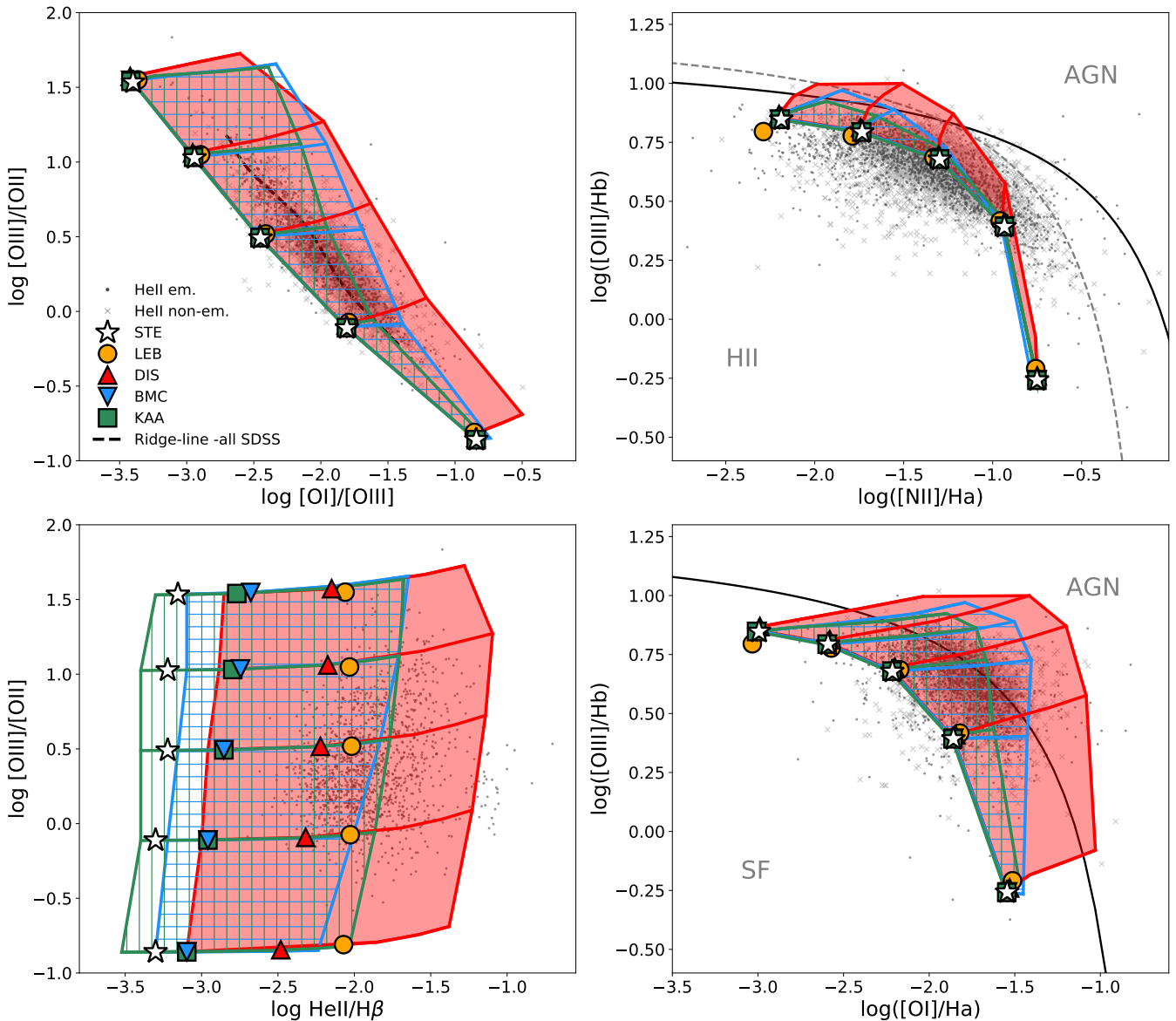


Fig. 4. Emission line ratio diagrams for our models ($\log U$ and L_X/SFR) for different SEDs compared to the observational sample. The left column shows high-ionisation emission line diagrams (see Stasińska et al. (2015)), while the right column shows low-ionisation diagrams (BPT diagram; e.g., Kewley et al. 2006; Baldwin et al. 1981). The points within a same model show the outputs obtained for the base models and different ionisation parameters. The shaded/coloured areas show the range of emission line ratios covered by the DIS, BMC and KAA models with varying X-ray luminosities and ionisation parameter. The lines show the results for a same ionisation parameter for each model (from top to bottom, $\log U = -1.5, -2.0, -2.5, -3.0, -3.5$) and increasing X-ray emission from left to right. For the stellar (STE) and the LEB SED the X-ray luminosity is constant by construction (and $L_X = 0$ for STE). The observational sample is shown by the grey symbols, where dots show the He II emitters and crosses the sources where He II is not detected. In approximately 2/3 of the galaxies HeII emission is not detected, with relative intensities below $I(4686)/I(H\beta) \sim (2 - 3) \times 10^{-3}$.

solar metallicity $\log L_X/SFR = 39.55 \pm 0.15$ (see e.g. Brorby et al. 2016), where nebular He II emission is generally not observed (cf. Guseva et al. 2000; Shirazi & Brinchmann 2012). Further observational studies are desirable to reach more firm conclusions (cf. below).

Senchyna et al. (2020) have done a similar modelling exercise as the present study, but have reached opposite results. They use spectra of HMXB from the multi-colour disc model (Mitsuda et al. 1984), which produces a modified blackbody spectrum representing gas at a range of temperatures in the accretion disc, and different black hole masses. These SEDs are then combined in the same way as in our study to the SED of integrated stellar populations, assuming variable amounts of L_X/SFR , and

then processed by Cloudy models. From their work, Senchyna et al. (2020) conclude that HMXBs are not efficient enough to produce the needed amount of He⁺ ionising photons, and hence that the HMXBs are not the dominant source of nebular He II in low-metallicity galaxies. The main differences with the present work are the adopted SEDs used to describe the X-rays sources. Clearly, the SEDs assumed by Senchyna et al. (2020) are very hard, and hence predict only small amounts of ionising photons close to the He⁺ ionisation potential. In other words their input spectra have a significantly lower Q_2/L_X than the ULX SEDs adopted here, which directly translates to lower He II $\lambda 4686/H\beta$ ratios for the same amount of X-ray emission (i.e. same L_X/SFR). The success or failure of their model and ours

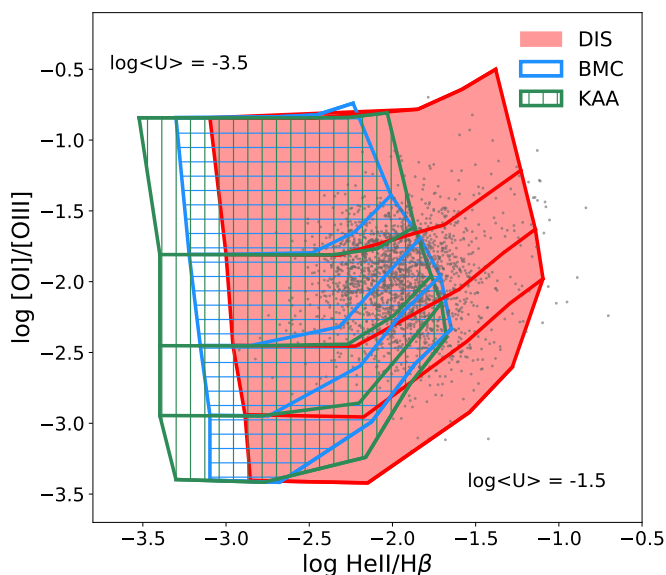


Fig. 5. Relation between $[OI]/[OIII]$ and $HeII/H\beta$ for the DIS, BMC and KAA models (shaded areas) along with the observational sample (dots). From top to bottom we show increasing ionisation parameter (lines). In approximately 2/3 of the galaxies $HeII$ emission is not detected, with relative intensities below $I(4686)/I(H\beta) \sim (2 - 3) \times 10^{-3}$.

therefore largely depends on the assumed X-ray SEDs which are adopted. We now discuss this issue and the diversity of SEDs among ULXs and HMXBs.

4.2. Diversity of SEDs among ULX

Early ULX observations were dominated by a single spectral component that could be fitted with accretion disk models (Makishima et al. 2000). However, as the spectral quality of observations improved with *Chandra* and *XMM-Newton*, it became evident that this single component model was not physically motivated and that deeper observations required more complex modelling (Kaaret et al. 2017).

A physically motivated ULX model would have two main components: an accretion disk modelled by radially dependent blackbodies and a Comptonised corona. The relative flux of these components varies, making the spectrum change its hardness (e.g. "soft UL" and "hard UL"; Sutton et al. 2013a,b). The fundamental properties of X-ray binaries are the mass, spin and nature of the compact object and companion star, as well as their orbital separation and eccentricity. The variation of these properties produces different SED shapes. In addition, as already discussed above, different components may be present (intermediate-mass BHs, irradiated disks, supercritical irradiated disks), and the mass-transfer rate is also expected to affect the intrinsic SEDs. Many studies suggest that ULXs correspond to a subset of sources with super-Eddington accretion rates seen basically face-on, whereas observations at high inclinations would see the enshrouded accretor as microquasars or super-soft sources (see Kaaret et al. 2017; Urquhart et al. 2019, and references therein).

Observationally, ULXs show emission across a wide spectral range, including in some cases radio emission and nebulae detected at optical and IR wavelengths, illustrating the many diverse associated processes (e.g. Cseh et al. 2014; Liu et al. 2015). In the case of nebulae, the detected emission lines may provide

useful information on the SEDs in the spectral range of interest here (primarily > 54 eV and up to the X-ray domain) and on contributions from other processes (e.g. shocks). Indeed, as already mentioned in the Introduction, numerous ULX nebulae showing high ionisation lines as $He II \lambda 4686$, $[Ne V] \lambda 3426$, and $[O IV]$ have been reported (e.g. Pakull & Mirioni 2002; Lehmann et al. 2005; Abolmasov et al. 2007, 2008; Kaaret & Corbel 2009; Berghea et al. 2010; Gris e et al. 2011; Maggi et al. 2011; Moon et al. 2011; Berghea & Dudik 2012; Binder et al. 2018; Urquhart et al. 2018; Vinokurov et al. 2018), but others do not show such lines (e.g. Pakull & Mirioni 2002; Abolmasov et al. 2007; D iaz Tello et al. 2017). Interestingly, some microquasars also show nebulae with $He II \lambda 4686$ emission (Pakull et al. 2010), another property in common with (some) ULX. Statistical results regarding the frequency and strength of these important lines have, to the best of our knowledge, not been reported. In any case, the present results point towards a diversity of the SED in the UV-to-X-ray domain.

Relatively few studies so far have examined ULX nebulae in classical BPT diagrams or used similar diagnostics to determine the dominant source of the optical emission (see e.g. Lehmann et al. 2005; Abolmasov et al. 2008). Recent examples of BPT diagrams are shown e.g. by (D iaz Tello et al. 2017), who find a ULX nebula located in the borderline between star forming and AGN regions. Another nebula is found in the LINER domain (L opez et al. 2019). The emission line ratios of the high-ionisation nebula Holmberg II X-1 are consistent with H II regions (Lehmann et al. 2005). According to Kaaret et al. (2017), most nebulae appear to be powered by shocks between outflows and the surrounding medium, while few are powered by photoionisation. Again, both X-ray/photo-ionised regions and shock-ionised nebulae seem to exist, but statistics and a more profound understanding of these nebulae is lacking.

In short, the variety and range of properties exhibited by ULXs make the modelling of ULXs a challenging task.

4.3. Other sources of nebular $He II$ emission

Several other processes and sources to explain nebular $He II$ emission in low-metallicity galaxies have been suggested and explored in the literature. These include for example shocks in the ISM and the existence of very hot stars, in addition to other "unconventional" suggestions.

Thuan & Izotov (2005), Izotov et al. (2012), and others have proposed that fast radiative shocks can explain both the observed $He II \lambda 4686$ and $[Ne V] \lambda 3426$ intensities in some low-metallicity galaxies. Using the shock models of Allen et al. (2008) for SMC and LMC metallicities, Izotov et al. (2012) show that the main intensities can be reproduced with shocks contributing $\sim 10\%$ of the total ionising flux, the rest being due to stars. Observed broad components in strong emission lines such as $H\alpha$ could be a direct observational signature indicating such shocks. The studies of Plat et al. (2019) and others reach similar conditions, arguing for shock or an AGN contribution to explain nebular $He II$. The principle difficulties of this scenario are probably to predict the required shock contribution in a quantitative manner, and to explain the observed increase of $He II/H\beta$ with decreasing metallicity. To the best of our knowledge this has not yet been addressed in the literature.

Basically since the discovery of frequent nebular $He II$ emission in low-metallicity galaxies, it has been shown that state-of-the-art evolutionary synthesis models combining the latest knowledge of stellar evolution and stellar atmospheres fall short of producing the high energy (> 54 eV) photons needed to repro-

duce this high ionisation line (see references in Sect. 1). Despite several updates, improvements, and the inclusion of stars resulting from stellar interactions in binary systems, this conclusion remains valid so far, as shown by several recent studies examining both the UV and/or optical He II recombination lines (e.g. Berg et al. 2018; Stanway & Eldridge 2019; Nanayakkara et al. 2019; Saxena et al. 2020a; Bian et al. 2020).

Despite this, several authors suggest that binary evolution, fast rotation or other processes could lead to very hot stars, which should boost and maybe provide sufficient He⁺ ionising photons (e.g. Götberg et al. 2019; Bian et al. 2020). However, no quantitative stellar population model solving this observational problem has been presented so far. Two recent studies propose that nebular He II emission with the observed intensities could even be achieved with conventional stellar populations, i.e. without the need to invoke other sources of higher energy photons. For example, Barrow (2019) performed cosmological zoom-in simulations of high-redshift galaxies including SEDs from the Flexible Stellar Population Synthesis code (FSPS Conroy & Gunn 2010) and following the evolution on very short timescales. In these simulations they identify several galaxies with He II λ 4686/H β \sim 0.001 – 0.03, which are found during specific, relatively short time intervals. The study of Barrow (2019) argues that gaps of \geq 15 Myr in star formation could explain the high intensities of He II without the need for other ionising sources.

However, in the detailed simulations which reach metallicities of $12 + \log(\text{O}/\text{H}) \lesssim 8.0$, comparable to those observed in the low- z galaxy sample, their models predict lower intensities (He II λ 4686/H β \lesssim 0.007) than the observations. Furthermore, the predicted He II phases occur only in sources with low H β equivalent widths ($\text{EW}(\text{H}\beta) \lesssim 10 \text{ \AA}$), in stark contrast with observations (see e.g. the compilation in Schaerer et al. 2019; Schaerer et al. 2020). Finally, the simulations predict only very few sources and short phases with nebular He II, again in contrast with the observations where nebular He II is detected in approximately $\sim 2/3$ of the star-forming galaxy samples at metallicities of $12 + \log(\text{O}/\text{H}) \lesssim 8.3$. From this we conclude that their model is not comparable to the observed low- z galaxy sample or that additional high-energy sources are indeed needed.

In a recent work, Pérez-Montero et al. (2020) have studied the behaviour of the nebular He I and He II lines in low- z galaxies and suggested that the observed intensities of He II could be explained by density-bounded H II regions powered by “normal” stellar SEDs. To achieve this with normal SEDs the relative He II λ 4686/H β predicted for Case B (ionisation bounded nebulae) must be significantly “boosted”. This can in principle be achieved by reducing a large fraction of the H β emission which is emitted quite uniformly across the entire H II region, whereas the central He II-emitting region remains unchanged. However, to reach the observed He II intensities, a very high mean escape fraction $f_{\text{esc}} = 0.74$ (or a mean absorption fraction 26 %) of the H ionising photons must be invoked (Pérez-Montero et al. 2020), which is not compatible with the observations. Indeed, overall Lyman continuum escape appears to be relatively rare and certainly well below this value at any redshift $z \lesssim 3$ where it has currently been measured (see e.g. Siana et al. 2015; Grazian et al. 2017; Steidel et al. 2018; Alavi et al. 2020). Also, at $z \sim 0.3 - 0.4$ where recent studies with HST have detected some Lyman continuum emitters, the measured escape fractions range from $\sim 2 - 70 \%$ (see e.g. Izotov et al. 2021, and references therein), with a mean escape fraction well below value invoked by Pérez-Montero et al. (2020). Furthermore, the known low- z leakers do not show different/enhanced He II/H β intensities (Gu-

seva et al. 2000). Finally, with such a large mean escape fraction the observed H β EW distribution of the He II emitters would be significantly altered (i.e. shifted to lower $\text{EW}(\text{H}\beta)$ by a factor ~ 4) and many He II emitters showing high $\text{EW}(\text{H}\beta)$ (cf. Shirazi & Brinchmann 2012; Schaerer et al. 2020) could hence not be explained by the same stellar population model which predict a maximum $\text{EW}(\text{H}\beta)$ which is quite close to the maximum observed value.

4.4. Future avenues

From the above discussions we conclude – based on our current knowledge of stars and stellar populations – that shocks, ULX/HMBX, a low-luminosity AGN contribution, or other sources of high energy photons are needed to solve the nebular He II problem. None of the existing scenarios provide so far fully satisfactory answers and/or quantitative results. Clearly, more research is needed to unveil the mystery of He II nebular emission.

For example, theoretical and observational studies to better understand the SEDs of ULX and HMXBs and their diversity might be of interest. Similarly, a better understanding of ULX nebulae, their frequency, observed spectra etc. would be useful. More generally, investigations on the impact of X-ray sources (both discrete and diffuse) on the ISM and observed spectra of star-forming galaxies may also shed new light on the He II problem and other, possibly related issues. Along these lines, several recent studies have e.g. investigated the link between X-rays and Ly α emitters, and possible connections between X-ray sources and Lyman continuum escape (see e.g. Sobral et al. 2015; Svoboda et al. 2019; Dittenber et al. 2020). More detailed investigations of shocks and their contribution of high ionisation lines, both on small scales (resolved) as well as in integrated galaxy spectra, would also seem of considerable interest.

The *James Webb Space Telescope* and other large telescopes will certainly continue to detect nebular He II emission in progressively more distant galaxies and provide invaluable new information on the stars, the ISM, and other components of galaxies in the early Universe. A proper solution of the long-standing nebular He II problem, which may affect other emission line diagnostics to a currently unknown extent, appears as a fundamental goal to confidently exploit these powerful new observations.

5. Conclusions

We have quantitatively examined the impact of luminous X-ray sources on the optical emission lines of star-forming galaxies and nebular He II in particular. To do so we have combined three empirically-constrained SEDs of ULXs with known nebulae from Berghea & Dudik (2012) and Kaaret & Corbel (2009) with the SED of stellar populations, as predicted from BPASS models (Eldridge et al. 2017). The X-ray luminosity of the source normalised to the SFR of the galaxy, L_X/SFR , is considered a free parameter, which is used to explore the effect of the X-ray sources. We varied L_X/SFR from 10^{39} to $\sim 10^{41} \text{ erg s}^{-1}/(\text{M}_{\odot} \text{ yr}^{-1})$, covering thus the range observed in star-forming galaxies (e.g. Mineo et al. 2014; Brorby & Kaaret 2017). Using the combined SEDs we have then computed Cloudy photoionisation models for conditions representative of low-metallicity galaxies from the sample of Guseva et al. (2019). Our main findings can be summarised as follows:

- The addition of X-ray emission from a ULX to a purely stellar SED hardens the spectrum of the galaxy, allowing a nebular He II emission with intensities up to He II λ 4686/H β \sim

0.04, comparable to the observations, with X-ray luminosities also compatible with observations. Increasing the X-ray contribution directly increases the output He II nebular emission.

- [Ne v] emission, which requires ionising photons with energies above 97.1 eV and is observed together with He II in a small number of blue compact dwarf galaxies, can be explained by the same models. The strong dependence of [Ne v] on the ionisation parameter can naturally explain why this line is only detected in a small fraction of He II emitters.
- The contribution of ULXs to the galaxy SED affects the classical optical diagnostic diagrams. As expected, the high energy radiation boosts both high and low ionisation lines. We show, e.g., that the BPT diagram involving [O I] $\lambda 6300/H\alpha$ is more significantly altered than [N II] $\lambda\lambda 6548, 6584/H\alpha$.
- We show that the main optical emission line ratios, involving three ionisation stages of Oxygen (namely [O III] $\lambda\lambda 4959, 5007$, [O II] $\lambda 3727$, and [O I] $\lambda 6300$), He II $\lambda 4686$, [N II] $\lambda\lambda 6548, 6584$, plus $H\alpha$ and $H\beta$, can consistently be reproduced by our galaxy SEDs including an ULX component.
- In particular, we have shown that the most efficient model is one in which an irradiated disc X-ray model is added, which can fit some ULXs both optical and X-ray wavelengths (DIS). The base spectra for the DIS model can achieve the observed percentage, while the BMC and KAA models are below expected.
- The impact of ULXs on the UV-optical emission lines of low-metallicity star-forming galaxies depends strongly on the shape of the SEDs of these X-ray sources, which are poorly known, most likely variable, and thus difficult to describe in an average sense.

Acknowledgements. We thank Ciprian Berghea, Philipp Kaaret, and Vianney Lebouteiller for communicating SEDs from their work. We also thank various colleagues, including Yuri Izotov, Aayush Saxena, Laura Pentericci, Tassos Fragos, Andrés Gúrpide, Lida Oskina, Nathalie Webb, Devina Misra, and John Chisholm for stimulating discussions on the nebular He II problem and ULXs during recent years. C.S and A.V. acknowledge support from SNF Professorship PP00P2_176808. A.V. is supported by the ERC starting grant ERC-757258-TRIPLE.

References

Abolfathi, B., Aguado, D. S., Aguilar, G., et al. 2018, *ApJS*, 235, 42
 Abolmasov, P., Fabrika, S., Sholukhova, O., & Afanasiev, V. 2007, *Astrophysical Bulletin*, 62, 36
 Abolmasov, P., Fabrika, S., Sholukhova, O., & Kotani, T. 2008, arXiv e-prints, arXiv:0809.0409
 Alavi, A., Colbert, J., Teplitz, H. I., et al. 2020, *ApJ*, 904, 59
 Allen, M. G., Groves, B. A., Dopita, M. A., Sutherland, R. S., & Kewley, L. J. 2008, *ApJS*, 178, 20
 Arnaud, K. A. 1996, in *Astronomical Society of the Pacific Conference Series*, Vol. 101, *Astronomical Data Analysis Software and Systems V*, ed. G. H. Jacoby & J. Barnes, 17
 Baldwin, J. A., Phillips, M. M., & Terlevich, R. 1981, *PASP*, 93, 5
 Barrow, K. S. S. 2019, *MNRAS*, 2947
 Berg, D. A., Chisholm, J., Erb, D. K., et al. 2019, *ApJ*, 878, L3
 Berg, D. A., Chisholm, J., Erb, D. K., et al. 2021, arXiv e-prints, arXiv:2105.12765
 Berg, D. A., Erb, D. K., Auger, M. W., Pettini, M., & Brammer, G. B. 2018, *ApJ*, 859, 164
 Berghea, C. T. & Dudik, R. P. 2012, *ApJ*, 751, 104
 Berghea, C. T., Dudik, R. P., Weaver, K. A., & Kallman, T. R. 2010, *ApJ*, 708, 364
 Bian, F., Kewley, L. J., Groves, B., & Dopita, M. A. 2020, *MNRAS*, 493, 580
 Binder, B., Levesque, E. M., & Dorn-Wallenstein, T. 2018, *The Astrophysical Journal*, 863, 141
 Brorby, M. & Kaaret, P. 2017, *MNRAS*, 470, 606
 Brorby, M., Kaaret, P., Prestwich, A., & Mirabel, I. F. 2016, *MNRAS*, 457, 4081
 Cassata, P., Le Fèvre, O., Charlot, S., et al. 2013, *A&A*, 556, A68

Conroy, C. & Gunn, J. E. 2010, *FSPS: Flexible Stellar Population Synthesis*
 Cseh, D., Corbel, S., Kaaret, P., et al. 2012, *The Astrophysical Journal*, 749, 17
 Cseh, D., Kaaret, P., Corbel, S., et al. 2014, *MNRAS*, 439, L1
 Díaz Tello, J., Miyaji, T., Ishigaki, T., et al. 2017, *A&A*, 604, A14
 Dittenber, B., Oey, M. S., Hodges-Klucck, E., et al. 2020, *ApJ*, 890, L12
 Douna, V. M., Pellizza, L. J., Mirabel, I. F., & Pedrosa, S. E. 2015, *A&A*, 579, A44
 Eldridge, J. J., Stanway, E. R., Xiao, L., et al. 2017, *PASA*, 34, e058
 Erb, D. K., Pettini, M., Shapley, A. E., et al. 2010, *ApJ*, 719, 1168
 Feltre, A., Charlot, S., Mignoli, M., et al. 2017, *Frontiers in Astronomy and Space Sciences*, 4, 32
 Ferland, G. J., Chatzikos, M., Guzmán, F., et al. 2017, *Rev. Mexicana Astron. Astrofis.*, 53, 385
 Fernández-Ontiveros, J. A., Spinoglio, L., Pereira-Santaella, M., et al. 2016, *ApJS*, 226, 19
 Fornasini, F. M., Kriek, M., Sanders, R. L., et al. 2019, *ApJ*, 885, 65
 Fragos, T., Lehmer, B., Tremmel, M., et al. 2013, *ApJ*, 764, 41
 Gierliński, M., Done, C., & Page, K. 2009, *MNRAS*, 392, 1106
 Gilfanov, M., Grimm, H. J., & Sunyaev, R. 2004, *MNRAS*, 347, L57
 Gladstone, J. C., Roberts, T. P., & Done, C. 2009, *MNRAS*, 397, 1836
 Gloczi, M., Titarchuk, L., Satyapal, S., Price, D., & Jang, I. 2011, *ApJ*, 735, 16
 Goad, M. R., Roberts, T. P., Reeves, J. N., & Uttley, P. 2006, *MNRAS*, 365, 191
 Göteborg, Y., de Mink, S. E., Groh, J. H., Leitherer, C., & Norman, C. 2019, *A&A*, 629, A134
 Grazian, A., Giallongo, E., Paris, D., et al. 2017, *A&A*, 602, A18
 Grevesse, N., Asplund, M., Sauval, A. J., & Scott, P. 2010, *Ap&SS*, 328, 179
 Grisé, F., Kaaret, P., Corbel, S., et al. 2012, *The Astrophysical Journal*, 745, 123
 Grisé, F., Kaaret, P., Pakull, M. W., & Motch, C. 2011, *ApJ*, 734, 23
 Gúrpide, A., Godet, O., Koliopanos, F., Webb, N., & Olive, J. F. 2021a, *A&A*, 649, A104
 Gúrpide, A., Godet, O., Vasilopoulos, G., Webb, N. A., & Olive, J. F. 2021b, arXiv e-prints, arXiv:2106.05708
 Guseva, N. G., Izotov, Y. I., Fricke, K. J., & Henkel, C. 2019, *A&A*, 624, A21
 Guseva, N. G., Izotov, Y. I., & Thuan, T. X. 2000, *ApJ*, 531, 776
 Izotov, Y. I., Guseva, N. G., Fricke, K. J., & Henkel, C. 2014, *A&A*, 561, A33
 Izotov, Y. I., Noeske, K. G., Guseva, N. G., et al. 2004, *A&A*, 415, L27
 Izotov, Y. I., Thuan, T. X., & Privon, G. 2012, *MNRAS*, 427, 1229
 Izotov, Y. I., Wörzner, G., Schaerer, D., et al. 2021, *MNRAS*, 503, 1734
 Ji, X., Yan, R., Riffel, R., Drory, N., & Zhang, K. 2020, *MNRAS*, 496, 1262
 Kaaret, P. & Corbel, S. 2009, *ApJ*, 697, 950
 Kaaret, P., Feng, H., & Roberts, T. P. 2017, *ARA&A*, 55, 303
 Kehrig, C., Guerrero, M. A., Vílchez, J. M., & Ramos-Larios, G. 2021, *ApJ*, 908, L54
 Kennicutt, Robert C., J. 1998, *ARA&A*, 36, 189
 Kewley, L. J., Groves, B., Kauffmann, G., & Heckman, T. 2006, *MNRAS*, 372, 961
 Kovlakas, K., Zezas, A., Andrews, J. J., et al. 2020, *MNRAS*, 498, 4790
 Laird, E. S., Nandra, K., Adelberger, K. L., Steidel, C. C., & Reddy, N. A. 2005, *MNRAS*, 359, 47
 Le Fèvre, O., Lemaux, B. C., Nakajima, K., et al. 2019, *A&A*, 625, A51
 Lebouteiller, V., Péquignot, D., Cormier, D., et al. 2017, *A&A*, 602, A45
 Lehmann, I., Becker, T., Fabrika, S., et al. 2005, *A&A*, 431, 847
 Lehmer, B. D., Basu-Zych, A. R., Mineo, S., et al. 2016, *ApJ*, 825, 7
 Lehmer, B. D., Eufrazio, R. T., Basu-Zych, A., et al. 2021, *ApJ*, 907, 17
 Liu, J.-F., Bai, Y., Wang, S., et al. 2015, *Nature*, 528, 108
 López, K. M., Jonker, P. G., Heida, M., et al. 2019, *MNRAS*, 489, 1249
 Madau, P. & Fragos, T. 2017, *ApJ*, 840, 39
 Maggi, P., Hou, X., & Pakull, M. 2011, in *The X-ray Universe 2011*, ed. J.-U. Ness & M. Ehle, 247
 Makishima, K., Kubota, A., Mizuno, T., et al. 2000, *ApJ*, 535, 632
 Middleton, M. J., Roberts, T. P., Done, C., & Jackson, F. E. 2011, *Monthly Notices of the Royal Astronomical Society*, 411, 644
 Miller, N. A., Mushotzky, R. F., & Neff, S. G. 2005, *ApJ*, 623, L109
 Mineo, S., Gilfanov, M., Lehmer, B. D., Morrison, G. E., & Sunyaev, R. 2014, *MNRAS*, 437, 1698
 Mineo, S., Gilfanov, M., & Sunyaev, R. 2012, *MNRAS*, 426, 1870
 Mitsuda, K., Inoue, H., Koyama, K., et al. 1984, *PASJ*, 36, 741
 Moon, D.-S., Harrison, F. A., Cenko, S. B., & Shariff, J. A. 2011, *ApJ*, 731, L32
 Nakajima, K., Schaerer, D., Le Fèvre, O., et al. 2018, *A&A*, 612, A94
 Nanayakkara, T., Brinchmann, J., Boogaard, L., et al. 2019, *A&A*, 624, A89
 Oskina, L. M., Bik, A., Mas-Hesse, J. M., et al. 2019, *A&A*, 627, A63
 Pakull, M. W. & Angebault, L. P. 1986, *Nature*, 322, 511
 Pakull, M. W. & Mirioni, L. 2002, arXiv e-prints, astro
 Pakull, M. W. & Mirioni, L. 2003, in *Revista Mexicana de Astronomía y Astrofísica Conference Series*, Vol. 15, *Revista Mexicana de Astronomía y Astrofísica Conference Series*, ed. J. Arthur & W. J. Henney, 197–199
 Pakull, M. W., Soria, R., & Motch, C. 2010, *Nature*, 466, 209
 Pérez-Montero, E., Kehrig, C., Vílchez, J. M., et al. 2020, arXiv e-prints, arXiv:2009.11076
 Pintore, F. & Mereghetti, S. 2016, *MNRAS*, 460, 1033

- Plat, A., Charlot, S., Bruzual, G., et al. 2019, MNRAS, 490, 978
- Poutanen, J. & Svensson, R. 1996, ApJ, 470, 249
- Raiter, A., Schaerer, D., & Fosbury, R. A. E. 2010, A&A, 523, A64
- Ramambason, L., Schaerer, D., Stasińska, G., et al. 2020, A&A, 644, A21
- Ranalli, P., Comastri, A., & Setti, G. 2003, A&A, 399, 39
- Rickards Vaught, R. J., Sandstrom, K. M., & Hunt, L. K. 2021, arXiv e-prints, arXiv:2104.03931
- Saxena, A., Pentericci, L., Mirabelli, M., et al. 2020a, A&A, 636, A47
- Saxena, A., Pentericci, L., Schaerer, D., et al. 2020b, MNRAS, 496, 3796
- Schaerer, D. 1996, ApJ, 467, L17
- Schaerer, D., Fragos, T., & Izotov, Y. I. 2019, A&A, 622, L10
- Schaerer, D., Izotov, Y., & Fragos, T. 2020, Proceedings of the International Astronomical Union, 15, 79
- Schaerer, D. & Stasińska, G. 1999, A&A, 345, L17
- Schmidt, K. B., Huang, K.-H., Treu, T., et al. 2017, ApJ, 839, 17
- Schmidt, K. B., Kerutt, J., Wisotzki, L., et al. 2021, arXiv e-prints, arXiv:2108.01713
- Senchyna, P., Stark, D. P., Mirocha, J., et al. 2020, MNRAS, 494, 941
- Senchyna, P., Stark, D. P., Vidal-García, A., et al. 2017, MNRAS, 472, 2608
- Shirazi, M. & Brinchmann, J. 2012, MNRAS, 421, 1043
- Siana, B., Shapley, A. E., Kulas, K. R., et al. 2015, ApJ, 804, 17
- Sobral, D., Matthee, J., Darvish, B., et al. 2015, ApJ, 808, 139
- Stanway, E. R. & Eldridge, J. J. 2019, A&A, 621, A105
- Stark, D. P. 2016, ARA&A, 54, 761
- Stark, D. P., Walth, G., Charlot, S., et al. 2015, MNRAS, 454, 1393
- Stasińska, G., Izotov, Y., Morisset, C., & Guseva, N. 2015, A&A, 576, A83
- Stasińska, G. & Tylenda, R. 1986, A&A, 155, 137
- Steidel, C. C., Bogosavljević, M., Shapley, A. E., et al. 2018, The Astrophysical Journal, 869, 123
- Steidel, C. C., Strom, A. L., Pettini, M., et al. 2016, ApJ, 826, 159
- Sturm, E., Lutz, D., Verma, A., et al. 2002, A&A, 393, 821
- Sutton, A. D., Roberts, T. P., Gladstone, J. C., et al. 2013a, MNRAS, 434, 1702
- Sutton, A. D., Roberts, T. P., & Middleton, M. J. 2013b, MNRAS, 435, 1758
- Svoboda, J., Douna, V., Orlitová, I., & Ehle, M. 2019, ApJ, 880, 144
- Székési, D., Langer, N., Yoon, S.-C., et al. 2015, A&A, 581, A15
- Tao, L., Kaaret, P., Feng, H., & Grisé, F. 2012, ApJ, 750, 110
- Thuan, T. X. & Izotov, Y. I. 2005, ApJS, 161, 240
- Titarchuk, L., Mastichiadis, A., & Kylafis, N. D. 1997, ApJ, 487, 834
- Urquhart, R., Soria, R., Johnston, H. M., et al. 2018, MNRAS, 475, 3561
- Urquhart, R., Soria, R., Pakull, M. W., et al. 2019, MNRAS, 482, 2389
- Vinokurov, A., Fabrika, S., & Atapin, K. 2018, ApJ, 854, 176
- Walton, D. J., Middleton, M. J., Rana, V., et al. 2015, ApJ, 806, 65

Appendix A: Comparison of Cloudy predictions with Case B

To first order, assuming simple case B recombination line emissivities, the relative line intensities of He II/H β is given by

$$I(4686)/I(H\beta) = A \times \frac{Q_2}{Q_0}, \quad (\text{A.1})$$

where Q_0 and Q_2 are the ionising photon fluxes for H and He⁺ respectively (i.e. above 13.6 and 54 eV), and $A \approx 1.74$ for typical nebular conditions (Stasińska et al. 2015). In Fig. A.1, we compare the line ratio calculated from this simple analytic expression with the predictions from our Cloudy model grid. Overall the scaling is as expected, and the models with high ionisation parameter agree well with Eq. A.1, except for very low values of He II/H β $\lesssim 3 \times 10^{-3}$, which is below the current detection limit. For models with low U , we find a decrease of He II/H β , by up to a factor $\sim 2 - 3$, which we attribute to the competition between H and He, discussed in earlier studies (e.g. Stasińska & Tylenda 1986; Raiter et al. 2010), and which cannot be captured by simple Case B theory. We also note that for the hardest SED (between 54 eV, the ionisation potential of He⁺, and the X-ray domain) Cloudy predicts a lower He II/H β intensity than naively expected from simple ionising-photon counting. This is most likely due to the fact only a fraction of photons with energy > 54 eV have energies sufficiently close to the ionisation potential to be efficiently absorbed by He⁺, whose photoionisation cross section decreases with ν^{-3} .

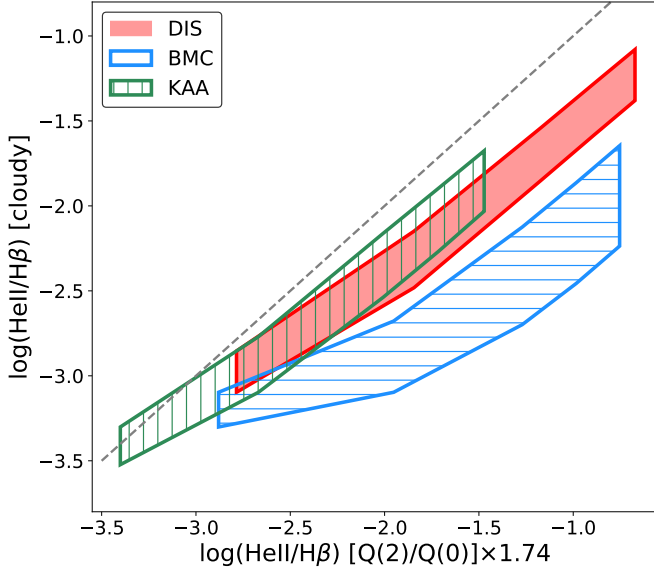


Fig. A.1. Percentages of HeII in relation to H β . The X-axis shows the analytical predictions based on the input spectra, where the factor 1.74 corresponds to typical nebular conditions. The dashed line shows a one-to-one relation between the predictions and the outputs. The upper and lower boundary for each model correspond to $\log U = -1.5$ and $\log U = -3.5$, respectively.